INTERNATIONAL JOURNAL FOR NUMERICAL METHODS IN FLUIDS, VOL. 14, 127–146 (1992)

TOWARDS THE NUMERICAL SIMULATION OF THE HORIZONTAL SLUG FRONT

N. YACOUB AND D. MOALEM MARON*

University of Tel-Aviv, School of Engineering, Ramat Aviv, 69978, Israel

AND

D. NAOT†

Center for Technological Education, POB 305, Holon 58102, Israel

SUMMARY

Steps towards the numerical simulation of the flow behind the slug front in horizontal slug flow performed with a streamfunction–vorticity representation of the mean flow and an energy dissipation model for the turbulence are discussed. The flow field consists of two vortices, one saddle point and four stagnation regions. Attention is focused on the following boundary conditions: moving wall jet, moving wall, free jet velocity discontinuity and vertical liquid–gas open surface. A dissipation flux boundary condition is suggested to simulate the interaction of the turbulent eddies with the open surface. A method to assess the necessity to use a transport model equation for the dissipation rather than a geometric specification of a length is suggested. Three different ways to characterize the mixing zone length are proposed.

KEY WORDS Numerical simulation Slug flow Turbulence Dissipation Open surface

1. INTRODUCTION

Two phase gas–liquid slug flow is characterized by intermittency and large velocity differences between the various regions. Consequently, slug flow incorporates a variety of hydrodynamic mechanisms with no single solution methodology applicable to all the regions of the field. A piecewise integral modelling was developed and tuned to the specific characteristics of the various zones: the slug liquid core, the slug trail gradually turning to a thin substrate, the elongated gas bubble moving fast ahead of the liquid slug front, etc. References 1–3 are but a few examples describing the horizontal slug flow and References 4–7 describe the modelling of the inclined and vertical slug flow. Unfortunately, the integral mechanistic modelling is incapable of accounting for the detailed distribution of the velocities, the wall shear stress, the turbulence energy, the energy dissipation and some other transport phenomena which are of special importance to the understanding of the slug frontal region. These were the subject of the study reported in Reference 8, where the numerical results were incorporated in a comprehensive model.

The following idealized flow configuration was assumed. The slug unit consists of a large lump of liquid steadily travelling over a continuous thin smooth substrate film. The velocity in the liquid slug is much greater than the mean velocity of the substrate film. Therefore a mixing eddy is

* At present: Director of Center for Technological Education
† Author to whom correspondence should be addressed.

0271–2091/92/020127–20$10.00

Received October 1989
Revised March 1991

formed at the slug front which picks up material from the substrate. Simultaneously, the slug sheds liquid from its back to form a decelerating trailing film. When the rate of liquid picked up at the front equals the rate of liquid shed at the rear, the length of the slug stabilizes. The existence of a fully developed region separating the slug front from its trailing film end was assumed, limiting the analysis somewhat. A co-ordinate system moving steadily with the slug front was used to perform the analysis. In such a system the substrate is fast moving and the slug front is stationary, forming a moving wall jet close to the wall and a free jet velocity discontinuity in the upper layers of the penetrating substrate.

The flow simulation was performed with a streamfunction–vorticity representation of the mean flow and an energy dissipation representation of the turbulence. Calculations were performed with a 20×80 grid with 20 vertically distributed nodes and 80 horizontally distributed nodes. Central point discretization was used for all the derivatives apart from the use of the upwind technique for the convective derivatives. The linearized finite difference equations were solved using the alternating direction implicit (ADI) integrator, which sweeps the grid, solving for a whole line (or column) with a tridiagonal matrix (TDM) inverter. Apparently, this was a straightforward simulation. Still, a few problems typical of this particular case had to be solved and are reported here.

The objectives of the present work stem from two aspects of the simulation: the expected conditions close to the moving solid walls, typical of the turbulent thin shear layer, and the use of the energy dissipation rate as a means for the description of the typical length scale.

Boundary conditions suitable for moving solid walls and the moving wall jet were formulated on the basis of the expected behaviour of the turbulent thin shear layer and are described here.

The logarithmic flow in local equilibrium adjacent to solid walls is characterized by singular vorticity, singular dissipation and linear variation of the turbulent eddy viscosity. These three features led to modifications in the vorticity equation. A special method designed to estimate the associated discretization errors is also discussed here.

The numerical simulation of the velocity discontinuity, which characterizes the penetration of the moving wall jet into the solution domain, raises doubts when use is made of the vorticity equation. A simple boundary condition representing the vorticity singularity is proposed and discussed here.

The boundary condition for the energy dissipation rate close to the open surface[9] was reconsidered and a flux condition for the dissipation at the vertical gas–liquid interface was developed on the basis of a phenomenological model for the renewal of the open surface structure. Application of this flux condition to the present study is also given here.

Performing a parametric study[8] associated with many repeated calculations obviously raises the wish to simplify the turbulence model. Here a method to assess the necessity to use a transport model for the dissipation rather than to specify a typical length scale on the basis of a simple and economic rule[10] is discussed in the light of the present study objectives.

Finally, selected calculated results for a typical horizontal slug flow frontal region are described. For the incorporation of the numerical simulations in the context of a comprehensive model for slug flow the reader is referred to Reference 8.

2. THE HYDRODYNAMIC MODEL

The hydrodynamic model for the horizontal slug front configuration shown in Figure 1 consists of a ψ–Ω representation for the mean flow and a $k-\varepsilon$ turbulence model. The mean velocity is related to the streamfunction by

$$\bar{U} = \partial\psi/\partial y, \qquad \bar{V} = -\partial\psi/\partial x, \tag{1}$$

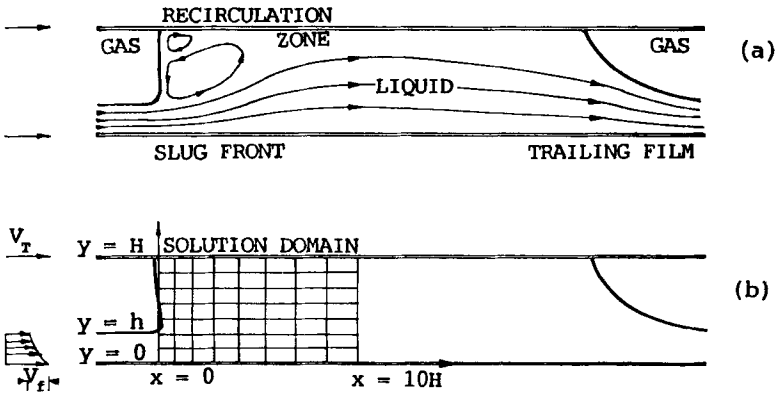

Figure 1. Horizontal slug front: (a) Expected flow configuration; (b) solution domain

satisfying the continuity equation for an incompressible fluid. With the vorticity defined as

$$\Omega = \partial \bar{V}/\partial x - \partial \bar{U}/\partial y, \tag{2}$$

the streamfunction becomes related to the vorticity by

$$\partial^2 \psi/\partial x^2 + \partial^2 \psi/\partial y^2 = -\Omega \tag{3}$$

and the vorticity transport equation takes the form

$$\bar{U}\frac{\partial \Omega}{\partial x} + \bar{V}\frac{\partial \Omega}{\partial y} = \frac{1}{\rho}\left[\left(\frac{\partial^2}{\partial x^2} - \frac{\partial^2}{\partial y^2}\right)\tau_{xy} + \frac{\partial^2}{\partial x \partial y}(\tau_{yy} - \tau_{xx})\right]. \tag{4}$$

The stresses are modelled by an effective scalar viscosity as

$$\frac{1}{\rho}\tau_{xy} = \nu_e\left(\frac{\partial \bar{U}}{\partial y} + \frac{\partial \bar{V}}{\partial x}\right), \tag{5a}$$

$$\frac{1}{\rho}(\tau_{yy} - \tau_{xx}) = \nu_e 2\left(\frac{\partial \bar{V}}{\partial y} - \frac{\partial \bar{U}}{\partial x}\right), \tag{5b}$$

and (4) becomes

$$\bar{U}\frac{\partial \Omega}{\partial x} + \bar{V}\frac{\partial \Omega}{\partial y} = \frac{1}{\nu_e}\left[\frac{\partial}{\partial x}\left(\nu_e^2 \frac{\partial \Omega}{\partial x}\right) + \frac{\partial}{\partial y}\left(\nu_e^2 \frac{\partial \Omega}{\partial y}\right)\right] + S_\Omega, \tag{6}$$

with the source term

$$S_\Omega = -\left[4\frac{\partial^2 \nu_e}{\partial x \partial y}\frac{\partial^2 \psi}{\partial x \partial y} + \left(\frac{\partial^2 \nu_e}{\partial x^2} - \frac{\partial^2 \nu_e}{\partial y^2}\right)\left(\frac{\partial^2 \psi}{\partial x^2} - \frac{\partial^2 \psi}{\partial y^2}\right)\right]. \tag{7}$$

In the above equations the effective viscosity

$$\nu_e = \nu_t + \nu \tag{8}$$

is related to the molecular viscosity ν and the turbulent eddy viscosity for high Reynolds number,

$$\nu_t = c_\mu k^2/\varepsilon, \tag{9}$$

where k is the turbulence energy and ε is the dissipation.

In this formulation the vorticity source S_Ω maintains symmetry between the role of the viscosity and the streamfunction, simplifying the accurate central difference discretization of this term. The non-linear use of the effective viscosity in the vorticity diffusion term increases the stability and accuracy of the discretization of this term as well. To see this, the alternative equation

$$\bar{U}\frac{\partial\Omega}{\partial x}+\bar{V}\frac{\partial\Omega}{\partial y}=\left[\frac{\partial}{\partial x}\left(\nu_e\frac{\partial\Omega}{\partial x}\right)+\frac{\partial}{\partial y}\left(\nu_e\frac{\partial\Omega}{\partial x}\right)\right]+S'_\Omega \tag{10}$$

and the associated source term

$$S'_\Omega=S_\Omega-\left[\frac{\partial\nu_e}{\partial x}\left(\frac{\partial^3\psi}{\partial x^3}+\frac{\partial^3\psi}{\partial x\partial y^2}\right)+\frac{\partial\nu_e}{\partial y}\left(\frac{\partial^3\psi}{\partial y^3}+\frac{\partial^3\psi}{\partial y\partial x^2}\right)\right] \tag{11}$$

should be noted. Equation (11) for the source term is more complicated than (7) since it contains third-order derivatives of Ψ, and is larger than (7) close to the walls since the first-order derivatives of ν_e are substantially larger than the second-order derivatives of ν_e. Since the source term is calculated on the basis of a previous iteration, transferring errors from that iteration, a reduction in the expected value of the source term enhances the numerical stability. The errors associated with the use of (6) for the present set-up are estimated in Section 6.

The turbulence transport model consists of an equation for the energy,

$$\bar{U}\frac{\partial k}{\partial x}+\bar{V}\frac{\partial k}{\partial y}=\left(\frac{\partial}{\partial x_i}\frac{\nu_e}{\sigma_k}\frac{\partial k}{\partial x_i}\right)+\pi-\varepsilon, \tag{12}$$

and a transport equation for the energy dissipation rate,

$$\bar{U}\frac{\partial\varepsilon}{\partial x}+\bar{V}\frac{\partial\varepsilon}{\partial y}=\left(\frac{\partial}{\partial x_i}\frac{\nu_e}{\sigma_\varepsilon}\frac{\partial\varepsilon}{\partial x_i}\right)+C_{\varepsilon1}\frac{\varepsilon}{k}\pi-C_{\varepsilon2}\frac{\varepsilon^2}{k}. \tag{13}$$

Here the energy production rate $\pi=-\overline{u_iu_j}\partial\bar{U}_i/\partial x_j$ is modelled by

$$\pi=\nu_t\left[2\left(\frac{\partial\bar{U}}{\partial x}\right)^2+2\left(\frac{\partial\bar{V}}{\partial y}\right)^2+\left(\frac{\partial\bar{U}}{\partial y}+\frac{\partial\bar{V}}{\partial x}\right)^2\right], \tag{14}$$

and C_μ, σ_k, σ_ε, $C_{\varepsilon1}$ and $C_{\varepsilon2}$ are the model coefficients. The examples shown in this work were calculated with the coefficients given in Table I, together with the Von Karmann constant χ.

Using a k–ε turbulence model, the length scale typical of the turbulent structure is not given directly. Instead, the high-Reynolds-number dissipation length scale

$$l=\frac{C_\mu^{3/4}}{\chi}\frac{k^{3/2}}{\varepsilon} \tag{15}$$

is used in conformity with (9) for the turbulent viscosity. The necessity to use a transport model equation for the dissipation rather than to specify a length scale for the turbulence using a geometric rule is not self-evident[10] and is considered in Section 7.

To accomplish the hydrodynamic model, the boundary conditions should be specified for the flow configurations demonstrated in Figure 2. Some conditions are of a technical nature and

Table I. Model coefficients

C_μ	σ_k	σ_ε	$C_{\varepsilon1}$	$C_{\varepsilon2}$	χ
0·09	1·225	1·225	1·44	1·92	0·40

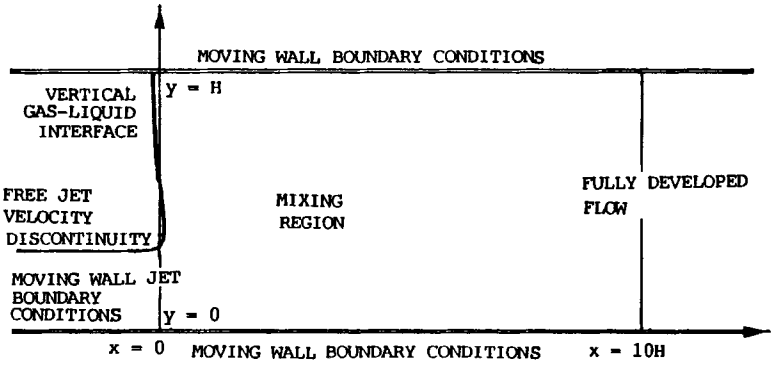

Figure 2. Various boundary conditions

define the input parameters. The co-ordinate system moves to the left with the vertical gas–liquid interface and therefore the walls move to the right at the same speed V_T, given as an input parameter. Owing to the relative motion between the slug and the substrate, a volumetric flow rate Q, given as an input parameter, is expected to enter the mixing region, the lower wall turning it to a moving wall jet the width of which, h, is equal to $Q/(V_T - V_f)$. Fully developed flow is assumed at the right boundary of the grid, restricting the simulation to flows where the recirculation zone is shorter than the mixing region. To avoid backflow, the field width H, also given as an input parameter, should not exceed a value of about $8Q/V_T$.

Some conditions, however, are typical of the slug front phenomena and are the subject of the present work. The moving wall jet forms a velocity discontinuity between the bulk of the wall jet and the recirculation zone, a situation discussed further in Section 3. With a vertical gas–liquid interface it is the surface tension that avoids spray of the turbulent eddies,[9] and the conditions developed for an open channel surface subjected to gravity are reassessed in Section 4. The moving wall boundary conditions are discussed in Section 5.

3. FREE JET VELOCITY DISCONTINUITY BOUNDARY CONDITION

Assuming a recirculation zone to exist in the liquid slug frontal zone, it is also expected that the two streamlines passing along the gas–liquid interface will merge to form the streamline joint configuration shown in Figure 3. Vorticity transport considerations, however, suggest that in the absence of internal vorticity sources and vorticity sources at the flow field boundaries, a recirculation zone can be predicted only by assuming a vorticity source at the streamline joint. A situation arises where the boundary condition for the cell that contains the free jet velocity discontinuity determines the whole field characteristics and therefore deserves consideration.

The vorticity convected through the left-side boundary into the first regular grid cell, shown in Figure 3, is

$$\int_a^b \bar{U}\Omega \,\mathrm{d}y = \int_a^b \bar{U}\left(\frac{\partial \bar{V}}{\partial x} - \frac{\partial \bar{U}}{\partial y}\right)\mathrm{d}y. \tag{16}$$

Since the main contribution to the integration is due to the singular behaviour of $\partial \bar{U}/\partial y$ at the velocity discontinuity, an approximation

$$\int_a^b \bar{U}\Omega \,\mathrm{d}y \simeq -\int_a^b \mathrm{d}\left(\frac{\bar{U}^2}{2}\right) \simeq \bar{U}_0^2 \frac{f}{2}, \tag{17}$$

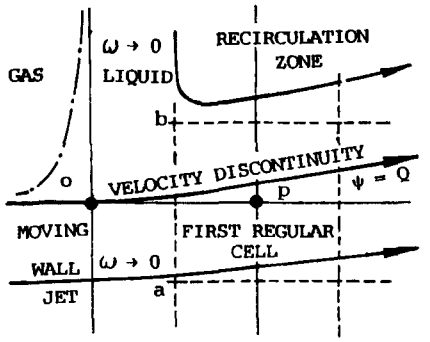

Figure 3. Streamline joint configuration and first regular cell

is suggested, with a parameter

$$f=(\bar{U}_a^2-\bar{U}_b^2)/U_0^2 \tag{18}$$

of the order of unity. To simulate this vorticity flux using a numerical procedure that accounts for the convection by

$$\int_a^b \bar{U}\Omega\,\mathrm{d}y=U_0\omega_0\Delta y, \tag{19}$$

it is necessary to use a representative vorticity

$$\omega_0=\frac{U_0}{2\Delta y}f \tag{20}$$

as a boundary condition at point 0. For small grid cell size Δy, ω_0 becomes unbounded, raising the question as to whether the integrated solutions converge to grid-independent results. In fact, experiments with a fine, 40×80, grid showed effects smaller than 1% for a decrease of 50% in Δy, indicating such a convergence.

On the other hand, considering a physical model, convergence to a singular solution raises doubts. Comparing a dynamic pressure build-up, ρV_T^2, to a pressure build up by surface tension, $\sigma/\Delta y$, with the grid size representing the surface curvature radius, one may state that a set-up with

$$\frac{\Delta y}{H}<\frac{\sigma}{\rho V_T^2 H} \tag{21}$$

ignores strong surface tension effects and is not acceptable. Therefore in the present study conditions the refinement of the grid is limited to 100 vertical nodes only.

The sensitivity of the streamline configuration to the specific choice of f is shown in Figure 4. With $f=1$ the streamlines close to the free jet discontinuity are parallel to the x-axis as expected. With smaller f, $f=0{\cdot}6$, they bend upwards, reducing the dimension of the vortex, and with larger f, $f=2$, they bend downwards, enlarging the vortex dimensions.

In certain set-ups the velocity discontinuity was positioned between two grids nodes. Substituting the representative vorticity at a single point led to the abnormal behaviour shown in Figure 5, typical of a lack of vorticity sources. Distributing the representative vorticity between the two cells adjacent to the velocity discontinuity in proportion to the distance to the grid nodes proved to be a useful practice, as is also shown in Figure 5.

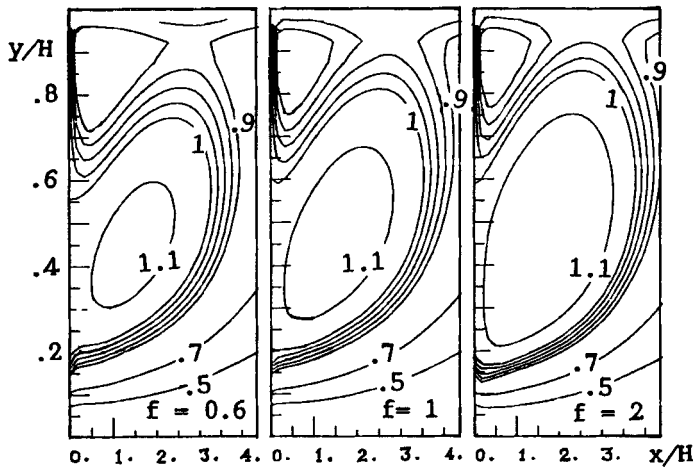

Figure 4. Sensitivity of streamlines to choice of f

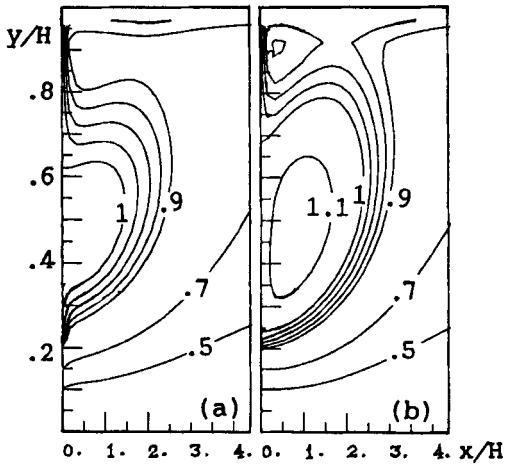

Figure 5. Calculated streamlines for representative vorticity (a) centred at a single 'wrong' cell and (b) split between two adjacent cells

4. SURFACE RENEWAL BOUNDARY CONDITIONS FOR THE DISSIPATION

The open surface boundary conditions for the k–ε turbulence model in channel flow[11,12] are adjusted here in order to cope with a vertical gas–liquid interface.[9]

The turbulent kinetic energy available for the formation of a new surface structure by a typical eddy moving from the flow field interior towards the interface is estimated by

$$E_a = \tfrac{1}{2} m \overline{v_n^2}, \tag{22}$$

where m is the typical eddy mass and v_n is the velocity fluctuation perpendicular to the interface.

Assuming the typical eddy to be a perfect sphere of diameter l, (22) becomes

$$E_a = \left(\frac{\pi}{12}\frac{\overline{v_n^2}}{k}\right)\rho l^3 k. \tag{23}$$

In the present model the open surface is assumed to remain unbreached. Hence, with the energy needed to overcome the surface tension and form droplets of the turbulent eddy's size given by

$$E_s = \pi l^2 \sigma, \tag{24}$$

the model is restricted to

$$E_a < E_s. \tag{25}$$

In terms of the local turbulence energy adjacent to the vertical open surface, (25) becomes

$$k < \frac{\sigma}{\rho l}\left(12\frac{k}{\overline{v_n^2}}\right). \tag{26}$$

With larger energy the onset of droplet spray is expected. Inequality (25) may also be formulated as a condition for the overall Weber number:

$$\rho\frac{\langle\bar{U}\rangle^2 H}{\sigma} < \left(12\frac{k}{\overline{v_n^2}}\right)\left(\frac{H}{l}\right)\left(\frac{\langle\bar{U}\rangle^2}{k}\right). \tag{27}$$

Estimating $l/H < 0.3$, $\overline{v_n^2}/k < \frac{2}{3}$ and $k/\langle\bar{U}\rangle^2 > 10^{-3}$, (26) and (27) become

$$\frac{\rho l k}{\sigma} < 18, \qquad \rho\frac{\langle\bar{U}\rangle^2 H}{\sigma} < 6\times 10^4 \tag{28}$$

respectively.

In the absence of energy-carrying droplets and assuming the open surface to function as an elastic membrane, the rejected eddy carries back into the flow field interior the energy E_a. The formation of an inward energy flux is common to both the vertical gas–liquid interface and the open surface of the channel, where gravity plays an important role:

$$\overline{J_k} = E_a/\tau\Delta s, \tag{29}$$

where τ is a typical time scale and Δs is a typical surface area. Assuming $\tau \simeq 1/(\overline{v_n^2})^{1/2}$ and $\Delta s = \pi l^2/4$, (29) becomes

$$\overline{J_k} = \left[\frac{1}{3}\left(\frac{\overline{v_n^2}}{k}\right)^{3/2}\right]\rho k^{3/2}. \tag{30}$$

With the inward energy flux being equal to the outward energy flux, the interface is energetically insulated:

$$\mathrm{d}k/\mathrm{d}x_n = 0. \tag{31}$$

However, owing to the open surface dynamics, the eddies rejected are correlated with the incoming eddies. Thus, when compared with a symmetry layer, the interface induces coherence and a higher collision density is expected in the liquid phase interior.[11]

To enhance dissipation additional to that expected adjacent to a symmetry layer, one may pose at the boundary a 'dissipation flux' condition. It is suggested to pose

$$\frac{\nu_e}{\sigma_\varepsilon}\frac{\mathrm{d}\varepsilon}{\mathrm{d}x_n} = \frac{\overline{J_k}}{\rho\tau} \tag{32}$$

and relate the dissipation flux to the inward energy flux doomed to dissipate owing to 'wrong timing'. Specifically, (32) becomes

$$\frac{\nu_\varepsilon}{\sigma_\varepsilon}\frac{d\varepsilon}{dx_n}=\left[\frac{1}{3}\left(\frac{\overline{v_n^2}}{k}\right)^2\right]\frac{k^2}{l}. \tag{33}$$

Using the high-Reynolds-number approximations for the dissipation diffusivity and length, (33) becomes a boundary condition for the dissipation,

$$\frac{d\varepsilon}{dx_n}=\alpha\frac{\varepsilon^2}{k^{3/2}}, \qquad \alpha=\frac{1}{3}\left(\frac{\overline{v_n^2}}{k}\right)^2\frac{\sigma_\varepsilon\chi}{C_\mu^{7/4}}, \tag{34}$$

or an alternative boundary condition for the length,

$$\frac{dl}{dx_n}=-\beta, \qquad \beta=\frac{1}{3}\left(\frac{\overline{v_n^2}}{k}\right)^2\frac{\sigma_\varepsilon}{C_\mu}. \tag{35}$$

Hossain and Rodi's condition[12] for open channel flow,

$$l=1{\cdot}07H-x_n, \tag{36}$$

was interpreted in References 13 and 14 as $l=0{\cdot}07H$ at $x_n=H$. However, with the alternative interpretation as $dl/dx_n=-1$, identified as the special case of (35) with $\beta=1$ and $\overline{v_n^2}/k=0{\cdot}456$, the consistent value of α becomes 2·43. Numerical calculation of one-dimensional open channel flow showed that the use of $\alpha=2{\cdot}43$ is indeed a good replacement for the $l=0{\cdot}07H$ condition. However, attempts to get better agreement with the data of Reference 15 shown in Figure 6 suggested $\alpha=3{\cdot}5$ ($\beta=1{\cdot}44$ and $\overline{v_n^2}/k=0{\cdot}546$).

The sensitivity of the horizontal slug flow simulations to the boundary conditions for the dissipation at the horizontal gas–liquid interface is demonstrated in Figure 7. The effect of the dissipation flux shows up when comparison is made with the insulated case $\alpha=0$. However, since the region influenced is almost stagnant, the overall effect on the streamfunction or the vorticity distribution is small in the present use.

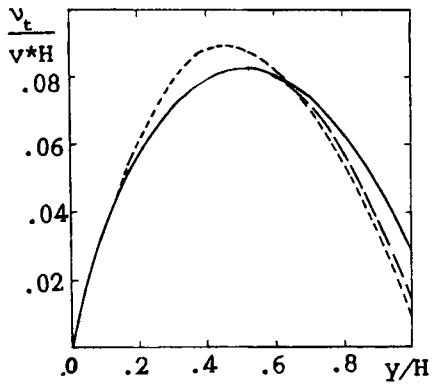

Figure 6. One-dimensional open channel flow:
---, Experimental data of Ueda *et al.*;[15]
——, Calculated, $\alpha=2{\cdot}43$;
– –, Calculated, $\alpha=3{\cdot}50$

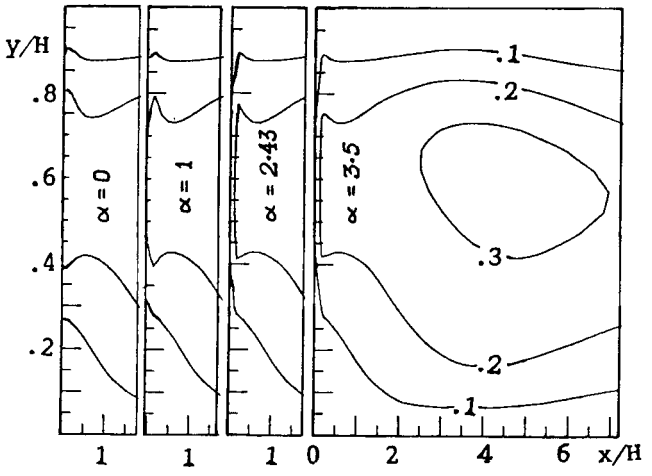

Figure 7. Influence of open surface boundary condition on dissipation length: l/H contours. $V_T H/\nu = 45\,700$

5. MOVING WALL BOUNDARY CONDITIONS

At each iteration the boundary conditions at the first grid line adjacent to the moving walls were updated following the thin shear layer assumptions. The flow close to solid walls is characterized by a logarithmic profile

$$\bar{U} = V_T - v_p^* 2{\cdot}5\left[\ln\left(\frac{v_p^* \eta}{\nu}\right) + 2\right], \tag{37}$$

where $v_p^* = v_B^*$ and $\eta = y$ for the bottom plate and $v_p^* = v_T^*$ and $\eta = H - y$ for the top plate. The streamfunction obtained by integration is

$$\psi_B = \int_0^y \bar{U}\,d\eta = y\left\{V_T - 2{\cdot}5 v_B^*\left[\ln\left(\frac{v_B^* y}{\nu}\right) + 1\right]\right\} \tag{38a}$$

for the bottom plate and

$$\psi_T = Q - \int_0^{H-y} \bar{U}\,d\eta = Q - (H-y)\left\{V_T - 2{\cdot}5 v_T^*\left[\ln\left(\frac{v_T^*(H-y)}{\nu}\right) + 1\right]\right\} \tag{38b}$$

for the top plate. Assuming vanishing V-component, the vorticity depends on $-d\bar{U}/dy$ only, yielding

$$\Omega_B = 2{\cdot}5 v_B^*/y \tag{39a}$$

for the bottom plate and

$$\Omega_T = -2{\cdot}5 v_T^*/(H-y) \tag{39b}$$

for the top plate. Owing to this assumption, the energy production degenerates to

$$\pi = -\overline{uv}\,d\bar{U}/dy. \tag{40}$$

The total shear stress typical of a thin shear layer is assumed to be constant. Therefore at $y^+ > 30$,

where the molecular stress is negligible, the turbulent stresses become

$$\overline{uv}_B = v_B^{*2} \quad \text{for the bottom plate,} \tag{41a}$$

$$\overline{uv}_T = -v_T^{*2} \quad \text{for the top plate.} \tag{41b}$$

The second important assumption is the local equilibrium assumption

$$\varepsilon = \pi, \tag{42}$$

used here together with the definition of the scalar eddy viscosity

$$\overline{uv} = -(C_\mu k^2/\varepsilon)\mathrm{d}\bar{U}/\mathrm{d}y. \tag{43}$$

Multiplying the left side of (43) by the right side of (40), multiplying the right side of (43) by π and using the local equilibrium condition (42), the turbulent energy is obtained as

$$k_p = (v_p^*)^2/C_\mu^{1/2}. \tag{44}$$

Substituting (41a, b) for the stresses and (39a, b) for $\mathrm{d}\bar{U}/\mathrm{d}y$ into the right side of (40) and using the local equilibrium condition (42), the energy dissipation is obtained as

$$\varepsilon_B = 2{\cdot}5(v_B^*)^3/y \quad \text{for the bottom plate,} \tag{45a}$$

$$\varepsilon_T = 2{\cdot}5(v_T^*)^3/(H-y) \quad \text{for the top plate.} \tag{45b}$$

The numerical solution was matched with the expected wall behaviour by taking values of ψ from the second grid line, solving (38a, b) iteratively for v_*. With known v_*, (38a, b), (39a, b), (44) and (45a, b) were used to update the boundary values of ψ, Ω, k and ε at the first grid node.

The inlet moving wall jet conditions are also based on the thin shear layer approximations. Although the moving wall jet penetrates the solution domain at $0<y<h$, $x=0$, with almost unified velocity, a small depletion in the velocity, V_f, always exists due to an interaction with the gas bubble. The depletion V_f is smaller than V_T and is also given as an input parameter. Owing to this small depletion, the non-zero vorticity, the turbulence energy and the dissipation exist at this important boundary. These were estimated assuming the velocity to show a logarithmic profile accompanied by local equilibrium turbulence.

Equation (38a) for $\psi(h) = h(V_T - V_f) = Q$ yields

$$V_f = 2{\cdot}5v_I^*\left[\ln\left(\frac{v_I^* h}{\nu}\right)+1\right] \tag{46}$$

to be solved iteratively for the inlet shear velocity v_I^*. Equations (39a), (38a), (44) and (45a) were used to estimate the vorticity, the streamfunction, the turbulence energy and the dissipation over the whole moving wall jet cross-section.

6. THE NUMERICAL ALGORITHM

The calculations were performed with a 20×80 grid with 20 nodes distributed evenly in the range $0<y<H$ and 80 nodes distributed with variable spacing in the range $0<x<10H$. The locations of the nodes were obtained by transforming x to an evenly distributed auxiliary variable z:

$$x = 10H(\mathrm{e}^z - 1)/(\beta^{M-1}-1), \quad 0<z<(M-1)\ln\beta. \tag{47}$$

With (47) the ratio between any $\Delta X_{n+1}/\Delta X_n$ is equal to β, taken here as 1·005.

Generally, the central point discretization was used to derive the finite difference formulation of all the terms apart from the convection terms simulated by the upwind technique. For more details see Appendix I. The finite difference equations were then organized in a form amenable to an alternating direction implicit (ADI) integrator. To this end, the values of the source terms, the values of the linearized terms and the values of the variables needed at grid nodes which are not on the particular line integrated were taken from the former iteration. With these preparations the grid was swept four times—upwards, downwards, to the right and to the left, not necessarily in that order—at each iteration. At each sweep, solutions were obtained for a whole line, line after line, with a tridiagonal matrix (TDM) inverter.

Once the mean flow equations for Ω and ψ had been solved, new velocities were calculated, updating the convection operator. Once the turbulence model equations for k and ε had been solved, the new turbulent viscosity was calculated and the effective viscosity was updated. Still, to avoid divergence at the early stage of the calculation, this updating process was underrelaxed during the first 50 iterations. With this practice it was possible to reduce the errors in satisfying locally the discretized equations for ψ and Ω to 10^{-5} times typical values for these variables, within 150 iterations or 600 grid sweeps consuming 400 s CPU time on a CDC 6600 computer.

To estimate the discretization error, a method based on the observation that close to the walls (39) for Ω and (45) for ε show singular character and are the source for large discretization errors was used. To estimate these errors, it was found useful to replace to original variables by new ones, $\Omega' = \Omega y$ and $\varepsilon' = \varepsilon y$, and solve close to the walls for the new variables, with further increase in accuracy obtained by replacing the effective viscosity by $\nu' = \nu_e / y$.

In the present set-up the errors in the wall shear velocity due to discretization are expected to be smaller than 3%. For details see Appendix II.

7. LENGTH SCALE DYNAMICS

The necessity to use a transport model for the dissipation rather than a geometric specification of a length scale is assessed. To this end, a transport equation for the length is derived by multiplying (12) by $C_\mu^{1/2}\sigma_k^3/2\varepsilon\chi^2$ and (13) by $C_\mu^{1/2}\sigma_\varepsilon k/\chi^2\varepsilon^2$ and subtracting the results:

$$\frac{\sigma_\varepsilon}{C_\mu^{1/4}\chi k^{1/2}}\frac{\mathrm{D}}{\mathrm{D}t}l = \left[l^2\frac{\partial}{\partial x_i}\left(\frac{1}{l}\frac{\partial l}{\partial x_i}\right)+1\right]+F_1+F_2+F_3+F_4+F_5, \tag{48}$$

where

$$F_1 = \frac{C_\mu^{1/2}\sigma_\varepsilon}{\chi^2}(C_{\varepsilon 2}-C_{\varepsilon 1})-1, \tag{49a}$$

$$F_2 = \frac{C_\mu^{1/2}\sigma_\varepsilon}{\chi^2}(\tfrac{3}{2}-C_{\varepsilon 1})\left(\frac{\pi}{\varepsilon}-1\right), \tag{49b}$$

$$F_3 = \frac{3}{2}\frac{C_\mu^{1/2}\sigma_\varepsilon}{\chi^2}\left(1-\frac{\sigma_k}{\sigma_\varepsilon}\right)\left[\frac{1}{\varepsilon}\frac{\partial}{\partial x_i}\left(\frac{\nu_t}{\sigma_k}\frac{\partial k}{\partial x_i}\right)\right], \tag{49c}$$

$$F_4 = -\frac{3}{4}\frac{l^2}{k^2}\left(\frac{\partial k}{\partial x_i}\right)\left(\frac{\partial k}{\partial x_i}\right), \tag{49d}$$

$$F_5 = \frac{7}{2}\frac{l}{k}\left(\frac{\partial k}{\partial x_i}\right)\left(\frac{\partial l}{\partial x_i}\right). \tag{49e}$$

The objective of this particular transformation is the observation that with vanishing F_i, $i = 1$–5,

and for fully developed flow, (48) degenerates to a form

$$l^2 \frac{\partial}{\partial x_i}\left(\frac{1}{l}\frac{\partial l}{\partial x_i}\right)+1=0, \tag{50}$$

which yields geometric solutions that depend on the field geometry and boundary conditions only. For example, for a closed duct of width H, (50) predicts the plausible geometric length scale

$$l=\frac{H}{\pi}\sin\left(\frac{\pi}{H}y\right). \tag{51}$$

Adjacent to the wall the geometric scale shows the $l=y$ behaviour maintained by the standard choice of the model coefficients that sets F_1 equal to zero.

The two parameters F_2 and F_3 reflect the influence of the absence of local equilibrium on the spectral structure. The parameter F_2 expresses the inequality between the energy production and dissipation. Assuming the energy production to be associated with an increase in the large-eddy population, F_2 is expected to become a source in the dissipation length scale equation in regions where an excess in energy production prevails. Indeed, (49b) predicts such a trend for $C_{\varepsilon 1}<1{\cdot}5$. With the standard choice of the model coefficients the effect is not pronounced. For example, away from shear layers π/ε becomes small and F_2 changes to a sink of about $-0{\cdot}13$ only.

The parameter F_3 expresses the ratio between the supply of energy by turbulent diffusion and the loss by dissipation. Assuming the large eddies to contribute to the turbulent energy diffusion more than the smaller ones, F_3 is expected to become a source in the length scale equation in regions where energy supply by turbulent diffusion prevails. Indeed, (49c) predicts such a trend for $\sigma_\varepsilon>\sigma_k$. Equation (49c) also explains the sensitivity of the numerical simulations to the difference $\sigma_\varepsilon-\sigma_k$: for $\sigma_\varepsilon-\sigma_k$ exceeding the small value $1-\frac{2}{3}C_{\varepsilon 1}=0{\cdot}04$, $|F_3|$ becomes larger than $|F_2|$; for $\sigma_\varepsilon-\sigma_k=0{\cdot}356$, $|F_3|$ becomes of the order of unity. With the choice of $\sigma_\varepsilon=\sigma_k$ used in Reference 8, this effect was minimized.

The two parameters F_4 and F_5 reflect the influence of the energy heterogeneity; for homogeneous turbulence both F_4 and F_5 vanish. By definition, F_4 is always a sink in the length equation. F_5, however, may change its sign. Close to the channel walls F_5 becomes a sink. Estimations for F_4 and F_5 based on the geometric scale and an approximation for the energy[10]

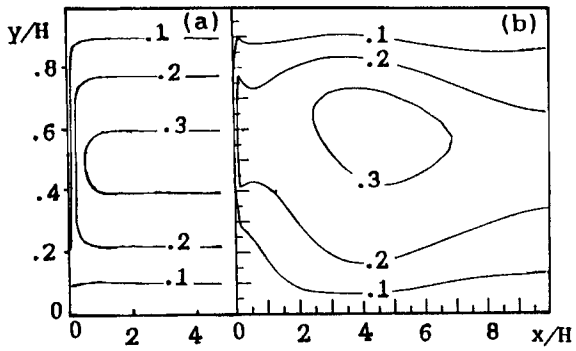

Figure 8. Horizontal slug front dissipation length scale:
(a) Geometric scale;
(b) calculated with k–ε model.
$V_T H/\nu = 45\,700$

show high values of the order of unity. It also appears that $|F_5|$ is the dominant parameter among the five F_i.

Finally, a comparison between the geometric scale calculated with (50) and the scale calculated with the full k–ε model is shown in Figure 8 for the horizontal slug flow configuration. At the right side of the domain the length calculated with the k–ε model becomes similar to the scale of the one-dimensional closed duct, which is 40% smaller than the geometric scale,[10] as expected. However, in the recirculation zone an effect of a large source, presumably due to F_5, is evident, reducing the difference between the two scales. The deviations between the geometric length scale and the calculated scale, owing to local conditions, are too large and the use of the full transport model is justified.

8. SELECTED RESULTS

Selected results of a numerical solution performed for the set of flow parameters given in Table II are now described.

The complexity of the horizontal slug flow field is probably best demonstrated by the streamlines shown in Figure 9, where contours for the ratio ψ/Q are given. Two vortices are induced at the slug front by the two moving walls. However, since the lower wall is accompanied by a wall jet, the vortex induced is the dominant one. Still, the second vortex shows up. Four stagnation zones are enforced. The first is found between the two vortices at the vertical gas–liquid interface. The second is formed between the large lower vortex and the upper moving wall and is referred to as a saddle point. Note that the centres of the two vortices are also stagnant; the total sum of stagnation zones induced by the two vortices is four.

The vorticity contours shown in Figure 10 for $\Omega H/V_T$ demonstrate the vorticity sources. The effect of a large source due to the velocity discontinuity boundary condition shows up, accompanied by a vorticity convection by the lower large vortex into the flow field interior. Close to the wall the contours merge with contours that represent the high level of vorticity induced by the logarithmic shear layer used as a boundary condition.

The turbulence energy contours shown in Figure 11 for $100k/V_T^2$ demonstrate the relative importance of the energy-producing regions. Here the shear layers that accompany the lower large vortex starting at the velocity discontinuity turn out to be the major energy source in the field, producing a high level of energy in the recirculation zone. The energy level induced by the logarithmic layers adjacent to the moving walls starting at the left side of the domain is relatively low. At the right end of the field, however, these sources remain the only energy sources and a situation typical of channel flow is formed where the energy is supplied to the dissipative central zone by turbulent diffusion from the walls.

Three scales representing the vortex length were also calculated: the distance from the entrance that the $\psi = Q$ line enveloping the vortex reaches, $l\psi$; the furthest point at which backflow is still detected, lu; the distance from the entrance at which the high dissipation rate averaged in a vertical cross-section differs by more than 5% from the fully developed value, ld. The dependence of these scales on the h/H ratio is shown in Table III and the influence of the Reynolds number HV_T/ν is shown in Table IV.

Table II. Flow field parameters

H (cm)	h (cm)	$Q \times 100$ ($m^2 s^{-1}$)	V_T ($m s^{-1}$)	V_f ($m s^{-1}$)
1	0·154	0·570	4·57	0·867

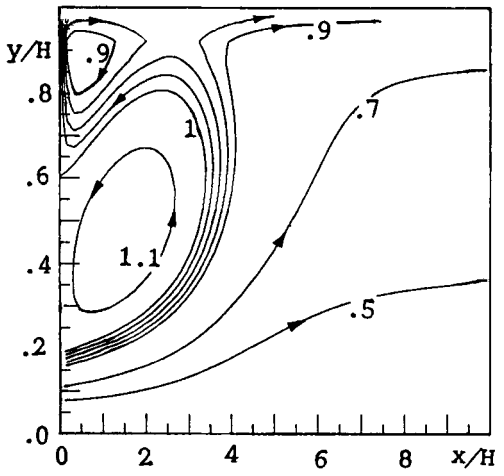

Figure 9. Horizontal slug front streamlines pattern: ψ/Q. $V_T H/\nu = 45\,700$

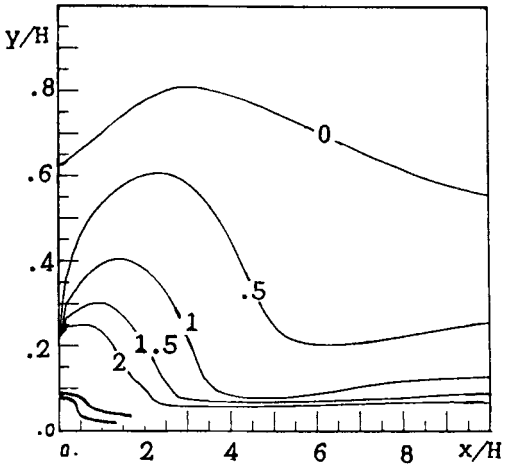

Figure 10. Horizontal slug front vorticity pattern: $\Omega H/V_T$. $V_T H/\nu = 45\,700$

The vortex core enveloped by the $\psi = Q$ line, represented by $l\psi$, is indeed smaller than the region where backflow is induced by the vortex, represented by lu. A high dissipation rate, however, characterizes a slightly larger domain: ld is almost equal to lu regardless of the flow conditions. A substantial decrease in the vortex dimensions with h/H ratio increase and a moderate increase in the vortex dimensions with Reynolds number HV_T/ν increase were detected. The interpretation of these findings in terms of the slug flow parameters is extended in Reference 8.

Another important outcome of the simulation is the local wall shear stress shown in Figure 12 for the two walls. The shear stress at the lower wall develops monotonically from the low values typical of the almost uniform flow that characterizes the moving wall jet at its entrance to the solution domain, to the higher values typical of the Poiseuille flow that develops at the right side of the domain. The flow adjacent to the upper plate, however, starts with a velocity discontinuity

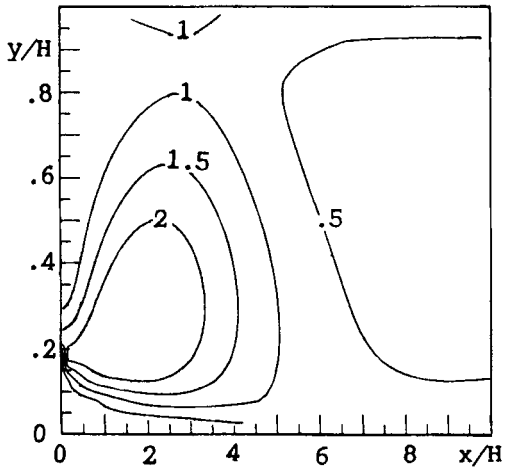

Figure 11. Horizontal slug front energy of turbulence: $k/0{\cdot}01V_T^2$. $V_T H/\nu = 45\,700$

Table III. Influence of h/H ratio on vortex length; $HV_T/\nu = 39\,000$

h/H	0·15	0·20	0·25	0·30	0·35
$l\psi/H$	3·47	2·68	1·78	1·08	0·82
$lu/l\psi$	1·32	1·43	1·84	2·57	3·05
ld/lu	1·02	1·07	1·15	1·17	1·19

Table IV. Influence of Reynolds number HV_T/ν on vortex length; $h/H = 0{\cdot}15$

HV_T/ν	23000	39000	69000	149000
$l\psi/H$	3·40	3·47	3·75	3·99
$lu/l\psi$	1·34	1·32	1·25	1·19
ld/lu	0·94	1·02	1·03	1·05

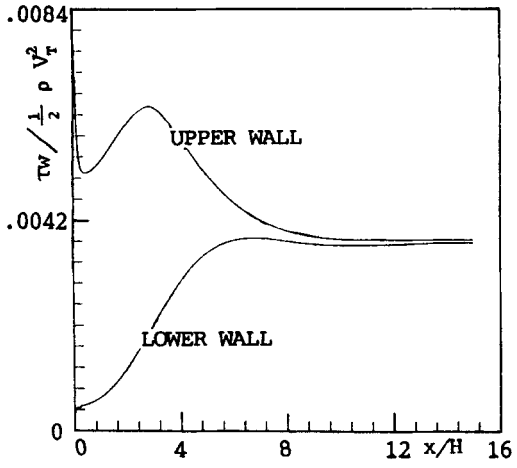

Figure 12. Horizontal slug front local wall shear stress. $V_T H/\nu = 45\,700$

followed by very high shear stress reducing rapidly by the upper vortex, and is then increased again to a local maximum due to the saddle point.

9. CONCLUDING REMARKS

The dissipation flux boundary condition suggested here and applied successfully to the horizontal open surface in channel flow was found to be an essential and useful tool for the vertical open surface. Although in the present case it influenced a region smaller than the vortex core, with limited overall effects, it is believed that the condition will also be found useful in other cases of non-horizontal open surfaces. It should be easy to extend the concept of dissipation flux to cases where, owing to droplet spray, the inward energy flux becomes smaller than the outward energy flux, thus reducing the dissipation flux.

A method to estimate the deviations of the dissipation length scale from a pure geometric behaviour, owing to the turbulent dynamic processes, was outlined, with two major outcomes. The use of the transport model equation for the dissipation was justified for the present case, and the choice of the k–ε turbulence model was criticized on the basis of the dissipation length scale dynamics. Further study in that direction may lead to the replacement of the dissipation transport model equation by either a pure geometric equation for the length scale for studies with less restricted demands for accuracy, or by the full transport model equation for the length scale for studies where reference to the spectral dynamics is essential and better understood.

The representative vorticity used here as the boundary condition for the numerical simulation of the free jet discontinuity at the boundary yields a reasonable streamline pattern, thus justifying the use of this simple condition. However, since the quality of the simulation depends strongly on a singular cell, it is felt that better understanding of the dynamics of that region is needed to dispense with the plausibility of the streamline pattern as a major argument.

The finite difference discretization and the ADI numerical solution are straightforward procedures. However, two issues were dealt with. Since the turbulent viscosity gradients are large and the second derivatives are not, the vorticity equation was rearranged in a way that increases the stability and makes the source terms simple, accurate and relatively small. The relatively large discretization errors due to the singular behaviour typical of the turbulent flow close to the walls were estimated using a special discretization technique.

Two different modes of behaviour of the wall shear stress were shown. The lower wall is characterized by a monotonic increase in the stress and the upper wall shows the characteristics of a leading edge of a boundary layer followed by a stress relaxation due to the upper vortex and then a stress build-up due to the saddle point. The averaged stress of both plates, however, is practically equal to the stress typical of a fully developed situation. This is an important observation which is expected to facilitate the analytic modelling of such two-phase flows.

Three methods to identify the vortex dimensions were suggested and studied, showing a dramatic decrease with h/H ratio increase and a moderate increase with Reynolds number increase. As expected, the region where backflow prevails is substantially larger than the vortex core and is characterized by a relatively high energy dissipation rate. These observations are also of importance for the analytic modelling of two-phase flows.

APPENDIX I: FINITE DIFFERENCE DISCRETIZATION

The streamfunction equation (4) becomes

$$A_E\psi_E + A_W\psi_W + A_N\psi_N + A_S\psi_S + A_C\psi_C = -\Omega_C, \tag{52}$$

where

$$A_E = A_W = 1/\Delta x^2, \tag{53}$$

$$A_N = A_S = 1/\Delta y^2, \tag{54}$$

$$A_C = -(A_E + A_W + A_N + A_S). \tag{55}$$

The vorticity equation (8) becomes

$$B_E\Omega_E + B_W\Omega_W + B_N\Omega_N + B_S\Omega_S + B_C\psi_C = S_\Omega, \tag{56}$$

where

$$B_E = C_E - \tfrac{1}{2}(v_E^2 + v_C^2)/v_C\Delta x^2, \tag{57}$$

$$B_W = C_W - \tfrac{1}{2}(v_W^2 + v_C^2)/v_C\Delta x^2, \tag{58}$$

$$B_N = C_N - \tfrac{1}{2}(v_N^2 + v_C^2)/v_C\Delta y^2, \tag{59}$$

$$B_S = C_S - \tfrac{1}{2}(v_S^2 + v_C^2)/v_C\Delta y^2, \tag{60}$$

$$B_C = -(B_E + B_W + B_N + B_S) \tag{61}$$

and S_Ω is the central point finite difference discretization of (9).

The energy equation (12) and the dissipation equation (13) become

$$D_E k_E + D_W k_W + D_N k_N + D_S k_S + D_C k_C = S_k, \tag{62}$$

$$D_E \varepsilon_E + D_W \varepsilon_W + D_N \varepsilon_N + D_S \varepsilon_S + D_C \varepsilon_C = S_\varepsilon, \tag{63}$$

respctively, where

$$D_E = C_E - \tfrac{1}{2}(\nu_E + \nu_C)/\sigma\Delta x^2, \tag{64}$$

$$D_W = C_W - \tfrac{1}{2}(\nu_W + \nu_C)/\sigma\Delta x^2, \tag{65}$$

$$D_S = C_S - \tfrac{1}{2}(\nu_S + \nu_C)/\sigma\Delta y^2, \tag{66}$$

$$D_N = C_N - \tfrac{1}{2}(\nu_N + \nu_C)/\sigma\Delta y^2, \tag{67}$$

$$D_C = -(D_E + D_W + D_N + D_S). \tag{68}$$

In (64)–(67) σ should be replaced by either σ_k or σ_ε in order to solve for the energy or the dissipation respectively. The source terms

$$S_k = \pi - \varepsilon_C, \tag{69}$$

$$S_\varepsilon = C_{\varepsilon 1}\varepsilon_C\pi/k_C - C_{\varepsilon 2}\varepsilon_C^2/k_C \tag{70}$$

were calculated using the central point discretization of (14) for π.

In the above equations the coefficients C represent the upwind convection scheme:

$$C_E = \tfrac{1}{2}(U_E - |U_E|)/\Delta x, \tag{71}$$

$$C_W = -\tfrac{1}{2}(U_W + |U_W|)/\Delta x, \tag{72}$$

$$C_N = \tfrac{1}{2}(V_N - |V_N|)/\Delta y, \tag{73}$$

$$C_S = -\tfrac{1}{2}(V_S + |V_S|)/\Delta y. \tag{74}$$

APPENDIX II. WALL PROXIMITY DISCRETIZATION ERRORS

Substituting the expected singular formulae $\Omega=\Omega'/y$, $\varepsilon=\varepsilon'/y$ and $v_e=v'y$ in the diffusion terms of (8) and (13) yields

$$\frac{\partial}{\partial y}\left(v_e^2\frac{\partial\Omega}{\partial y}\right)=y\frac{\partial}{\partial y}\left(v'^2\frac{\partial\Omega'}{\partial y}\right)-\Omega'\frac{\partial}{\partial y}(v'^2), \tag{75}$$

$$\frac{\partial}{\partial y}\left(v_e\frac{\partial\varepsilon}{\partial y}\right)=\frac{\partial}{\partial y}\left(v'\frac{\partial\varepsilon'}{\partial y}\right)-\frac{1}{y}\frac{\partial}{\partial y}(v'\varepsilon')+\frac{1}{y^2}(v'\varepsilon'). \tag{76}$$

Applying the central finite difference scheme to the right-hand side of these equations rather than to the left-hand side is expected to yield smaller discretization errors since Ω', ε' and v' are expected to become almost constant close to the wall. Therefore the formulae thus obtained with the original variables Ω, ε and v_e resubstituted, i.e.

$$\frac{\partial}{\partial y}\left(v_e^2\frac{\partial\Omega}{\partial y}\right)=\frac{1}{2}\left(v_N^2\frac{y_C}{y_N}+v_C^2\frac{y_N}{y_C}\right)\frac{1}{\Delta y^2}\Omega_N+\frac{1}{2}\left(v_S^2\frac{y_C}{y_S}+v_C^2\frac{y_S}{y_C}\right)\frac{1}{\Delta y^2}\Omega_S$$
$$-\frac{1}{2}\left(v_N^2\frac{y_C}{y_N}+v_S^2\frac{y_C}{y_S}+2v_C^2\right)\frac{1}{\Delta y^2}\Omega_C, \tag{77}$$

$$\frac{\partial}{\partial y}\left(v_e\frac{\partial\varepsilon}{\partial y}\right)=\frac{1}{2}\left(v_N\frac{y_S}{y_C}+v_C\frac{y_N}{y_C}\right)\frac{1}{\Delta y^2}\varepsilon_N+\frac{1}{2}\left(v_S\frac{y_N}{y_C}+v_C\frac{y_S}{y_C}\right)\frac{1}{\Delta y^2}\varepsilon_S$$
$$-\frac{1}{2}\left(v_N\frac{y_C}{y_N}+v_S\frac{y_C}{y_S}+2v_C\frac{y_Ny_S}{y_C^2}\right)\frac{1}{\Delta y^2}\varepsilon_C, \tag{78}$$

are expected to be more accurate close to the walls than the original formulae

$$\frac{\partial}{\partial y}\left(v_e^2\frac{\partial\Omega}{\partial y}\right)=\tfrac{1}{2}[(v_N^2+v_C^2)]\frac{1}{\Delta y^2}\Omega_N+\tfrac{1}{2}[(v_S^2+v_C^2)]\frac{1}{\Delta y^2}\Omega_S-\tfrac{1}{2}[(v_N^2+v_S^2+2v_C^2)]\frac{1}{\Delta y^2}\Omega_C, \tag{79}$$

$$\frac{\partial}{\partial y}\left(v_e\frac{\partial\varepsilon}{\partial y}\right)=\tfrac{1}{2}[(v_N+v_C)]\frac{1}{\Delta y^2}\varepsilon_N+\tfrac{1}{2}[(v_S+v_C)]\frac{1}{\Delta y^2}\varepsilon_S-\tfrac{1}{2}[(v_N+v_S+2v_C)]\varepsilon_C. \tag{80}$$

Obviously, away from walls, (79) and (80) are more accurate. Comparison of runs with (77) and (78) applied to the cells close to the walls in the domain $30<y^+<200$ with runs where (79) and (80) were applied throughout the calculation domain may serve as an indication of the discretization errors stemming from the wall proximity.

REFERENCES

1. A. E. Dukler and M. G. Hubbard, 'A model for gas–liquid slug flow in horizontal and near horizontal tubes', *Ind. Eng. Chem. Fund.*, **14**, 337–347 (1975).
2. M. K. Nicholson, K. Aziz and G. A. Gregory, 'Intermittent two phase flow in horizontal pipes: predictive models', *Can. J. Chem. Eng.*, **56**, 653–663 (1978).
3. D. M. Maron, N. Yacoub and N. Brauner, 'New thoughts on the mechanism of gas–liquid slug flow', *Lett. Heat and Mass Transfer*, **9**, 333–342 (1982).
4. R. H. Bonnecaze, W. Eriskine Jr. and E. J. Greskovich, 'Holdup and pressure drop for two-phase slug flow in inclined pipelines', *AIChE J.*, **17**, 1109–1113 (1971).
5. R. C. Fernandes, R. Semiat and A. E. Dukler, 'Hydrodynamic model for gas–liquid slug flow in vertical tubes', *AIChE J.*, **29**, 981–989 (1983).
6. A. Orell and R. Rembrand, 'A model for gas–liquid slug flow in a vertical tube', *Ind. Eng. Chem. Fund.*, **25**, 196–206 (1986).

7. N. D. Sylvester, 'A mechanistic model for two phase vertical slug flow in pipes', *J. Energy Resources Technol.*, **109,** 206–213 (1987).
8. D. Maron Moalem, N. Yacoub, N. Brauner and D. Naot, 'Hydrodynamic mechanisms in horizontal slug pattern', *Int. J. Multiphase Flow*, **17**(2), 227–246 (1991).
9. D. Naot, N. Yacoub and D. Maron Moalem, 'Open surface renewal boundary conditions for the k–ε turbulence model', *Proc. 23rd Conf. of the IAHR, Vol. A*, International Association of Hydraulic Research, Ottawa, 1989, pp. 293–299.
10. D. Naot, N. Yaçoub and D. Maron Moalem, 'Dissipation length scale dynamics', *Proc. 6th Beer Sheva Seminar on MHD—Flows and Turbulence*, February (1990).
11. D. Naot and W. Rodi, 'Interactions of the turbulent eddies with free surface', in Branover, Lykoudis and Yakhot (eds), *Liquid Metal Flow and MHD, AIAA Progress in Astronautics and Aeronautics, Vol. 84*, AIAA, New York, 1983, pp. 98–112.
12. M. S. Hossain and W. Rodi, 'Mathematical modelling of vertical mixing in stratified channel flow', *Proc. 2nd Symp. on Stratified Flows*, Trondheim, 1980.
13. D. Naot and W. Rodi, 'Calculation of secondary currents in channel flow', *J. Hydraul. Div. ASCE*, **108,** 948–968 (1982).
14. D. Naot, 'Response of channel flow to roughness heterogeneity', *ASCE J. Hydraul. Eng.*, **110,** 1568–1587 (1984).
15. H. Ueda, R. Moller, S. Komori and T. Mizushina, 'Eddy diffusivity near the free surface of open channel flow', *Int. J. Heat Mass Transfer*, **20,** 1127–1136 (1977).